Effect of a Zr source addition on the microstructure of Al-SiC composites elaborated by the Laser Powder Bed Fusion (L-PBF) process

Marie-Reine Manlay, Camille Flament, Stéphane Gossé, Mathieu Soulier, Jean-Paul Garandet

Materials Characterization 218 (2024) 114472

Contents lists available at ScienceDirect

Materials Characterization

journal homepage: www.elsevier.com/locate/matchar

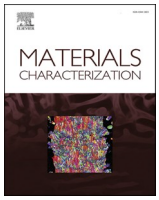

Effect of a Zr source addition on the microstructure of Al-SiC composites elaborated by the Laser Powder Bed Fusion (L-PBF) process

Marie-Reine Manlay [a], Camille Flament [a], Stéphane Gossé [b], Mathieu Soulier [a], Jean-Paul Garandet [a,*]

[a] Univ. Grenoble Alpes, CEA, LITEN, DTNM, F-38000 Grenoble, France
[b] Université Paris-Saclay, CEA, Service de Recherche en Corrosion et Comportement des Matériaux, 91191 Gif-sur-Yvette, France

ARTICLE INFO

Keywords:
SiC decomposition
Nucleation
Microstructure
L-PBF
Transmission electron microscopy
Calphad

ABSTRACT

The present work focuses on the effect of the addition of a zirconium source on the microstructure of Al-SiC composites produced by Laser Powder Bed Fusion (L-PBF). More specifically, the aim is to address the issue of the SiC decomposition into the water-soluble aluminum carbide Al_4C_3 in Al-SiC composites produced by L-PBF, with the objective of limiting its formation by adding another element to the system. To this end, $AlSi_7Mg_{0.6}$-SiC-ZrO_2 composite powders are successfully prepared and printed in a standard L-PBF equipment. The resulting parts are then thoroughly characterized, in order to understand the physico-chemical mechanisms involved during the L-PBF process. The results show a decrease in the Al_4C_3 amount by ZrC formation. Another important result is that bulk composites exhibit a fully equiaxed microstructure attributed to the τ_1 $(Al,Si)_3Zr$ ternary phase, with all the characteristics of a good nucleating agent for aluminum phase. To support these microstructure experimental results, a first version of a quaternary Al-Zr-Si-C thermodynamic database was developed using the Calphad method. These calculations enable to establish a solidification path providing information on the phases that may form after heat treatment of L-PBF materials.

1. Introduction

Laser Powder Bed Fusion (L-PBF) is one of the most mature methods in the rapidly developing field of metal additive manufacturing. It consists in the repetition of the selective laser fusion and solidification of metal powder beds according to a pre-defined scanning path, until the desired part is grown. This technique addresses the growing demand for high-density metal parts with complex geometries, fine and controlled microstructures. A major scientific and technical challenge, particularly in the transportation industry, is to reduce the weight of structures while maintaining the functional properties of parts, such as mechanical properties. In this respect, aluminum alloys are known to offer an excellent compromise between lightness and mechanical strength. The L-PBF process fits into this context of lightening structures by further topological optimization of parts. Moreover, many aluminum alloys, especially those with high silicon content, are well adapted for the implementation of this technique, since they are not prone to hot cracking issues.

According to the target application, it may be necessary to mechanically strengthen aluminum alloys by introducing reinforcements to form metal matrix composites. Aluminum matrix composites reinforced with silicon carbide particles are widely used in industrial applications, particularly in the automotive, aerospace and defense sectors [1]. They are attractive because of their low density, high mechanical strength and Young modulus, and corrosion resistance [2]. However, during the conventional production of these composites by stir-casting or infiltration, it is known that a chemical reaction can occur above 660 °C between the liquid aluminum and the SiC reinforcements, leading to the formation of an aluminum carbide, Al_4C_3, according to the following reaction [3].

$$4\,Al + 3\,SiC \rightarrow Al_4C_3 + 3\,Si \quad (1)$$

This carbide alters the mechanical properties and parts lifetime, due to its brittleness and tendency to hydrolyze [4]. In casting processes, a strict control of the temperature cycle and of the system chemistry allow to limit SiC decomposition. Unfortunately, the much higher

* Corresponding author.
E-mail addresses: camille.flament@cea.fr (C. Flament), stephane.gosse@cea.fr (S. Gossé), mathieu.soulier@cea.fr (M. Soulier), jean-paul.garandet@cea.fr (J.-P. Garandet).

https://doi.org/10.1016/j.matchar.2024.114472
Received 13 June 2024; Received in revised form 4 October 2024; Accepted 15 October 2024
Available online 19 October 2024

temperatures associated with L-PBF prevent these strategies from being effective. On the other hand, the kinetics of this process being much faster than those of casting or infiltration, our previous work investigated the issue of SiC decomposition in an $AlSi_7Mg_{0.6}$-SiC composite produced by L-PBF, with the aim of estimating whether this decomposition could be limited by the kinetics of the process [5]. Through a coupled experimental and numerical analysis, this previous study showed that submicron SiC particles could not survive the L-PBF process, resulting in the formation of Al_4C_3.

In this context, the objective of the present work is to develop an alternative approach to counteract the negative effects of SiC decomposition in Al-SiC composites produced by L-PBF. This consists in adding an element to an $AlSi_7Mg_{0.6}$-SiC composite powder to form another carbide than Al_4C_3. Based on a binary carbide stability diagram [6], our choice was zirconium because ZrC has a more negative Gibbs free energy than Al_4C_3. Although such stability diagrams of binary carbides do not take into account the ternary interactions of these carbides, they allow to identify the most energetically stable carbides, and can be used for purposes of first selection based on thermodynamic criteria. At this point, it should be stated that the Al-Zr-C ternary system studied by Schuster and Nowotny [7] indicates the absence of equilibrium between liquid aluminum and ZrC at 700 °C and 1000 °C. However, composition conditions can be locally satisfied to allow the formation of ZrC.

Indeed, Long et al. [6] showed that the mechanical properties reduction of a laser weld joint of two Al-SiC composite parts containing 10 vol% SiC, due to the expected degradation of SiC into Al_4C_3, could be alleviated by the addition of a 50 μm-thick zirconium foil between the two composite plates. With such an approach, the amount of porosity in the joint was reduced, and its mechanical strength increased. This effect is associated with the absence of Al_4C_3 precipitates and the formation of ZrC precipitates of about 5–10 μm in size, allowed by the local composition conditions around the zirconium foil, according to the following reaction:

$$SiC + Zr \rightarrow ZrC + Si \quad (2)$$

Therefore, the results of Long et al. [6] represented an interesting proof of concept of the possibility to limit the amount of Al_4C_3 by the in situ formation of ZrC during the process. Our objective in the present work is to adapt this strategy of Zr addition to the elaboration of Al-SiC based composites by L-PBF. In order to satisfy the objective of promoting the in situ formation of ZrC during the process in order to avoid the formation of Al_4C_3, it is necessary to introduce into the system a molar fraction of zirconium at least equal to the molar fraction of carbon from silicon carbide. Moreover, it could be profitable to introduce a molar excess of Zr, which could promote the formation of Al_3Zr, known to be an excellent nucleating agent in aluminum alloys [8–11].

Regarding the paper organization, the materials and methods used to perform this research work are detailed in Section 2. The results obtained are then presented and analyzed in Section 3. Finally, Section 4 is dedicated to a discussion of the findings, providing clues regarding the physico-chemistry of a new composite elaborated by L-PBF.

2. Materials and methods

2.1. Raw materials

The host material used in this study is gas atomized spherical $AlSi_7Mg_{0.6}$ powder acquired from TLS Technik GmbH & Co. The particles have a range size of 15–53 μm and a median diameter of 29 μm. Their chemical composition is reported in Table 1. The powder density, as measured by Helium pycnometry, is 2.66 $g{\cdot}cm^{-3}$.

As mentioned in the introduction, the aim of the present work is to add a zirconium source to an $AlSi_7Mg_{0.6}$-SiC composite powder. To this end, SiC nanoparticles with a mean size of 35 nm are used. These nanoparticles, provided by Nanomakers, are produced by laser pyrolysis.

Several zirconium sources can be selected to meet the desired objectives. In line with a previous study based on Al 6061 powders [8], a nanosized ZrO_2 powder with a characteristic particle size of 80 nm supplied by US Research Nanomaterials, was selected for its large availability and easy handling in order to produce an $AlSi_7Mg_{0.6}$-SiC-ZrO_2 ternary composite powder. Since the objective in the present work is to clarify complex physico-chemistry issues rather than to produce application-oriented materials, we decided to set the total content of reinforcements at 5 wt% in order to form a significant density of precipitates, making it easier the analysis of X-ray diffractograms. Two mixtures with different ratios R = [Zr]/[C] were prepared, one with $R = 1$ and the other with an excess of Zr, with $R = 3$. Their composition is presented in Table 2. These composite powders will be respectively named R1 and R3 afterwards.

2.2. Nanocomposite powders elaboration

The aim of the mixing step is to perform dry coating of nano-sized reinforcements on matrix particles. Dry coating is based on an electrostatic assembly of nanoparticles at the surface of micrometric powders [14]. The potential of this approach to develop nanocomposite powders for the L-PBF process has already been demonstrated in a previous work [15]. Composite powders mixtures with 5 wt% reinforcements are produced using a 5 L capacity Cyclomix high-shear mixer, with a rotation speed of 15 $m{\cdot}s^{-1}$ and a mixing duration of 30 min.

Composite powders properties are investigated through several characterization techniques. Powders granulometry is estimated using static image analysis (Malvern Morphologi G3), allowing to give information on the electrostatic mixture stability. The analysis is performed on 150,000 particles at a x20 magnification with a detection limit for particles smaller than 1 μm. The quality of electrostatic assembly of powders is also evaluated on secondary electron images taken from Scanning Electron Microscopy (SEM) using a Field Emission Gun (FEG) SEM Zeiss Merlin. For the determination of mass balances, Instrumental Gas Analysis (IGA) and Inductively Coupled Plasma (ICP) analysis, performed by Elektrowerk Weisweiler GmbH, were also used. IGA measurements for carbon are performed on 0.10–0.40 g samples, while ICP analysis are performed on 1 g samples.

2.3. Laser Powder Bed Fusion (L-PBF) process

Bulk composites are produced by Laser Powder Bed Fusion with a SLM Solutions machine (SLM 125 HL), equipped with a 400 W laser and

Table 2
Composition of composite powder mixtures.

R = [Zr]/[C]	R = 1	R = 3
Composite name	R1	R3
SiC content	1.23 wt%	0.49 wt%
ZrO_2 content	3.77 wt%	4.51 wt%

Table 1
Chemical composition of the $AlSi_7Mg_{0.6}$ alloy powder (wt%).

Composition	Al	Si	Mg	Fe	Cu	Zn	Ti	Mn
Specification	Bal.	6.50–7.50	0.45–0.70	≤0.19	≤0.05	≤0.07	0.08–0.25	≤0.10
Powder	Bal.	7.23	0.62	0.18	0.005	<0.001	0.18	0.003

a spot diameter of 70 μm, using the same procedure and the same process parameters than our previous work [5].

Based on these parameters, samples are identified according to their Energy per Built Volume (EBV) [16]. The density of bulk composites is then measured using the standard Archimedes' method in ethanol. In order to study the physico-chemistry of the composites produced, their microstructure is thoroughly characterized using a variety of methods. The different phases constituted the composite are identified by means of X-Ray Diffraction (XRD) (Bruker D8 Advance) with a variation of 2θ angle from 28° to 42°. Such a relatively restricted range was selected for time saving purposes. Nevertheless, we checked using larger acquisition intervals that it was adequate to identify the relevant phases within our samples. At an intermediate spatial scale, grains morphology and orientation are characterized tanks to SEM and Electron Backscatter Diffraction (EBSD). Energy Dispersive X-rays spectroscopy (EDX) analyses are performed to characterize precipitation. For SEM analyses, the electron acceleration voltage is set at 5 kV and the current at 1 nA for images and EDX analyses. EBSD maps are acquired by tilting the sample by 70° and applying a voltage of 20 kV and a current of 7 nA, with a pixel size of 100 nm. For a more detailed characterization, Transmission Electron Microscopy (TEM) analyses are performed using a FEG Tecnai Osiris from Thermofisher operating at 200 kV. The images are recorded by conventional TEM, or by S-TEM with High Angle Annular Dark Field (HAADF) and Bright Field (BF) detectors. EDX data are acquired in STEM mode with the super-X detector equipped with four Silicon Drift Detectors (SSD). Data are treated with Esprit 1.9 from Bruker Phase and orientation maps are performed by recording the diffraction pattern at each point with a camera thanks to ACOM-TEM. These patterns are automatically indexing using ASTAR software from NanoMEGAS. For details on this technique, the interested reader is referred to references [17, 18]. Acquisitions are conducted with a precessed beam with an angle of 1.2°. Beam size is of about 1 nm and 5 nm pixel. Samples for TEM analyses are prepared using a cross-beam Focused Ion Beam 550 from Zeiss (FIB). The characterized TEM lamellae are lifted out according to the perpendicular plane to building direction.

2.4. Thermodynamic assessment of the quaternary Al-Zr-Si-C system

In order to relate the experimental results obtained with thermodynamics, a first version of a thermodynamic database of the quaternary Al-Zr-Si-C system was developed using the Calphad method and Thermo-Calc package (2022b version). Although other chemical elements are present in the system, we selected to consider only the interactions between major elements Al, Si, Zr and C. The Calphad method allows to calculate phase diagrams and thermodynamic properties from the description of the Gibbs energy functions of all phases (solid, liquid and gas) in a given chemical system, and to make predictive calculations to investigate as yet unstudied temperature or composition domains.

The quaternary description is based six binary and four ternary subsystems, i.e. the Al—C, Al—Si, Al—Zr, C—Si, C—Zr and Si—Zr binaries and the Al-C-Si, Al-C-Zr, Al-Si-Zr and C-Si-Zr ternaries. Among these systems, all were already thermodynamically assessed but Al-C-Zr is poorly described experimentally. The description of the ternary Al-C-Si and sub-systems comes from Gröbner et al. [19]. This assessment considers two ternary intermetallics: Al_4C_4Si and Al_8C_7Si; both these phases are stoichiometric. The Al—Zr, Si—Zr and Al-Si-Zr thermodynamic descriptions come from Hirano et al. [12]. This study considers three ternary intermetallics noted τ_1, τ_2 & τ_3. They correspond to both line compounds $(Al,Si)_3Zr$ and (Al,Si)Zr and to the stoichiometric phase $Al_4Si_5Zr_3$. The C—Zr thermodynamic model is taken from Fernandez Guillermet [20]. No particular excess parameters were considered in the ternary C-Si-Zr.

The Al-C-Zr system is poorly described experimentally. Because no Calphad model exists for this ternary, a specific database was developed from limited information from the literature. The ternary isothermal sections were established from the diagrams by Schuster and Nowotny [7] who identified three intermetallics: Zr_5Al_3C, $ZrAlC_{2-x}$, and $Zr_2Al_3C_{5-x}$. Due to the lack of data, these two last phases were considered stoichiometric in the Calphad model. The formation enthalpy of these MAX phases were taken from DFT data of Poulou et al. [21]. No supplementary Al-C-Zr ternary phases were considered.

As the thermodynamic properties and stability domains of these Al-Zr-C ternary phases are not well known, this ternary system needs to be further investigated and considered with caution in view of the limited data available. This is also the case for the Al-Zr-Si ternary system, calculated from the Hirano et al. database [12], in which the description of ternary intermetallics appears to be only based on experimental results at 700 °C. On the other hand, the thermodynamic modeling of the other two ternary systems Al-Si-C [19] and Si-Zr-C [22] are considered very satisfying when compared to the experimental data.

It is important to keep in mind that the $AlSi_7Mg_{0.6}$ matrix used in this work has a high silicon content, which could lead to the formation of the τ_1 ternary line compound with $(Al,Si)_3Zr$ composition, rather than Al_3Zr [12,13]. In the quaternary system Al-Si-Zr-C, anticipating on the focus that will be on the τ_1 and ZrC phases, as well as their interaction with liquid aluminum, the ternary diagrams of interest are Al-Si-Zr and Al-Zr-C. Fig. 1 shows the isothermal cross-sections of Al-Zr-C and Al-Si-Zr ternary diagrams calculated at 1000 °C. The quaternary system is then extrapolated from the thermodynamic description of the four ternary subsystems.

Considering the isothermal section of the Al-Zr-C ternary diagram, it is interesting to note that among the ternary phases, two compounds, $Zr_2Al_3C_5$ and $ZrAlC_2$, are in equilibrium with the liquid phase, depending on its composition. The carbide ZrC_{1-x} is also in equilibrium with these ternary phases, depending on its stoichiometry, and zirconium aluminides, including Al_3Zr.

Considering the Al-Zr-Si isothermal cross-section, the presence of τ_1 and τ_2 ternary phases can be noted at 1000 °C, respectively defined as $Zr(Al_{1-x}Si_x)_3$ with $0.1 \leq x \leq 0.4$ and $Zr(Al_xSi_{1-x})$ with $0.2 \leq x \leq 0.25$ [13]. At this temperature, the main phases in equilibrium with the liquid phase, according to the liquid composition, are Al_3Zr, τ_1 and a $Si_2(Al,Zr)$ solid solution. This τ_1 phase is notably in equilibrium with the Al_3Zr phase, as well as τ_2, depending on the composition of τ_1.

2.5. Heat treatments

Thermal analyses are also performed to complement the calculations from the Calphad database, and to make the link with the results obtained after L-PBF. Differential thermal analysis (DTA) tests are used to estimate the formation temperatures of the various compounds. These measurements are carried out using a SETARAM TAG24 DTA, with a temperature ramp from 10 °C·min^{-1} from the ambient up to 1000 °C and an argon flow rate of 30 L·h^{-1}.

Moreover, heat treatment tests are carried out on composite powders in a Nabertherm tube furnace under argon flow. The temperature rise and cooling ramp is 250 °C·h^{-1}, and the sample is held at working temperature, i.e. 650 °C and 800 °C, for one hour.

3. Results

3.1. Composite powders characterization

Before focusing on the physico-chemistry of ternary $AlSi_7Mg_{0.6}$-SiC-ZrO_2 composites produced by L-PBF, it is necessary to characterize the electrostatic assembly of the SiC and ZrO_2 nanoparticles which ensures the stability and the homogeneity of the powder mixture.

The methodology used to characterize composite powders will not be detailed here. Further information are given in our previous work [5]. The aim is to ensure that the mixture is of sufficient quality for subsequent physico-chemical studies on composite parts. SEM images provide a first qualitative approach to qualify the electrostatic assembly. On the SEM images of R1 and R3 powders shown in the Supplementary data 1,

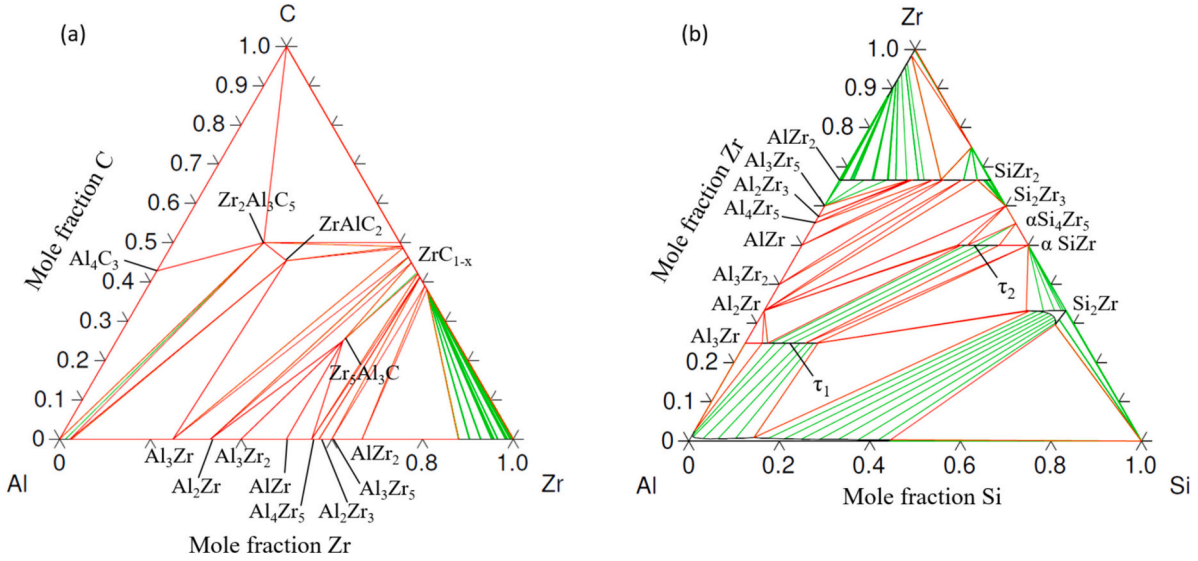

Fig. 1. (a) Al-Zr-C and (b) Al-Si-Zr isothermal cross-sections at 1000 °C.

the nanoparticles appear to completely cover the surface of the aluminum particles, as evidenced by their fluffy surface appearance. No segregation of free nanoparticles is observed in the powder samples analyzed by SEM. To complete these results, granulometry results show a monomodal size distribution of the composite powders, as that of the matrix powder, indicating a complete electrostatic assembly (Supplementary data 2). Indeed, if this were not the case, the size distribution of the powder would be modified by the presence in the mixture of SiC and ZrO_2 ungrafted particles, self-agglomerated because of their high specific area, detectable by a second peak.

Table 3 displays IGA and ICP measurements on C and Zr elements in the composite powders, compared with their theoretical quantity introduced into the mixture.

The values presented for the R1 composite powder correspond to an average value obtained from three samples taken from a 250 mL powder volume, while a single sample was analyzed for the R3 composite. From the three measurements carried out on the R1 composite powder, standard deviations in absolute values of respectively of 0.01 wt% and 0.08 wt% were obtained for the elements C and Zr. As such a dispersion is of the order of the error linked to the measurement techniques themselves, which are 0.01 pds% for carbon and 0.06 pds% for zirconium, it is not possible to highlight any differences that might be due to the heterogeneous distribution of SiC and ZrO_2 powders. In conclusion, the composite powders produced appear suitable for investigating the fate of these particles after L-PBF.

3.2. Microstructure characterization

Density measurements using the Archimedes' method (Supplementary data 3) allow to select the sample printed at a EBV of 32.6 J·mm^{-3} among the densest for the subsequent microstructural study, measured at 2.53 g·cm^{-3}. Since no relevant reference density values can be obtained in such complex multiphase systems, the results are presented in absolute, i.e. g·cm^{-3}. The porosity rate is then estimated by optical microscopy on polished sections of samples R1 and R3, by image binarization on an analysis area of 13.5 mm^2. This analysis indicates a porosity rate of around 6 % in both composites. Numerous porosities can be observed, both irregular and spherical in shape. However, although the composites would require process optimization to reduce the porosity, the microstructure seems to be similar between the porosities, allowing to carry out the study of the physicochemistry of composites on these areas.

Table 3
Analysis of carbon and zirconium content in the composite powders compared to their expected content.

Composite	R1		R3	
Element	C	Zr	C	Zr
Powder (wt%)	0.35	2.30	0.12	3.14
Theory (wt%)	0.37	2.79	0.15	3.38

According to EBSD analysis of Al-SiC bulk composites from our previous study, the microstructure of Al-SiC composites elaborated by L-PBF mainly consists of columnar grains textured ⟨100⟩ in the building direction (Supplementary data 4). On the contrary, R1 and R3 composites with the addition of ZrO_2 display a completely equiaxed microstructure, as shown in Fig. 2. This figure also shows the presence of numerous intragranular and intergranular Zr-rich precipitates. Compared with Al-SiC composites and their columnar grains, the microstructure is highly refined, with a linear grain size of around 1 μm. The formation of this totally equiaxed microstructure may implies the presence of a nucleating agent for the aluminum phase. The goal now is to identify the precipitation in the bulk samples, and to identify the germinating agent involved.

Fig. 3 displays the X-ray diffractograms obtained on the bulk composites R1 and R3 obtained at a EBV of 32.6 J·mm^{-3}.

The diffractograms of composites R1 and R3 both exhibit peaks characteristic of the diffraction of the ZrC phase. This result reflects the successful in situ synthesis of ZrC during the L-PBF thermal cycle undergone by the material. The objective of trapping the released carbon with zirconium has thus been at least partially achieved. However, the absence of peaks characteristic of Al_4C_3 diffraction does not certify the absence of Al_4C_3 in the material, as it can be present in insufficient amounts to be detected. Nevertheless, the detection of the ZrC phase necessarily implies a reduction in Al_4C_3 formation. Both composites also show peaks associated with the diffraction of the ternary Al-Zr-Si τ_1 phase.

The τ_1 phase appears to have been formed preferentially to the Al_3Zr phase, as this phase widely documented in the literature is undetected and not observed by electron microscopy. This appears to be due to the high silicon content present in the $AlSi_7Mg_{0,6}$ matrix, since similar tests carried out with pure Al or Al 6061 matrix show Al_3Zr precipitation [23]. This result was also highlighted by Gao et al. [24], although in another manufacturing process. Furthermore, the fact that the τ_1 phase is identified in the R1 composite, which contains as much zirconium as carbon, means that there are less zirconium atoms available to form ZrC,

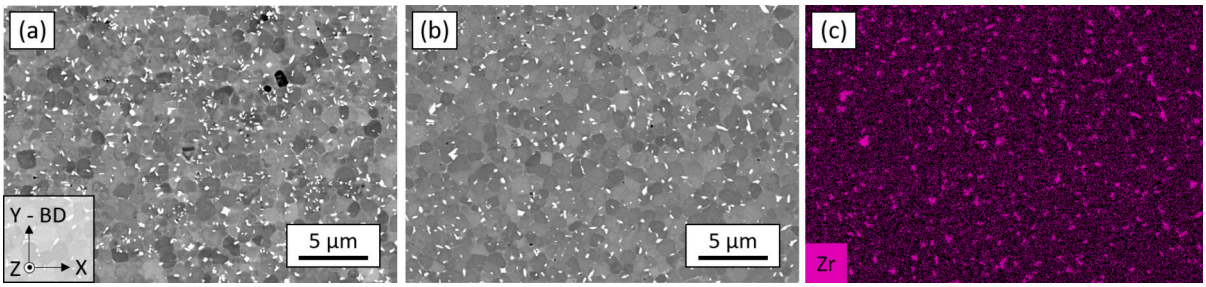

Fig. 2. (a) SEM-BSE image of R1 microstructure, (b) SEM-BSE image of R3 microstructure, (c) EDX analysis for Zr in R3 composite.

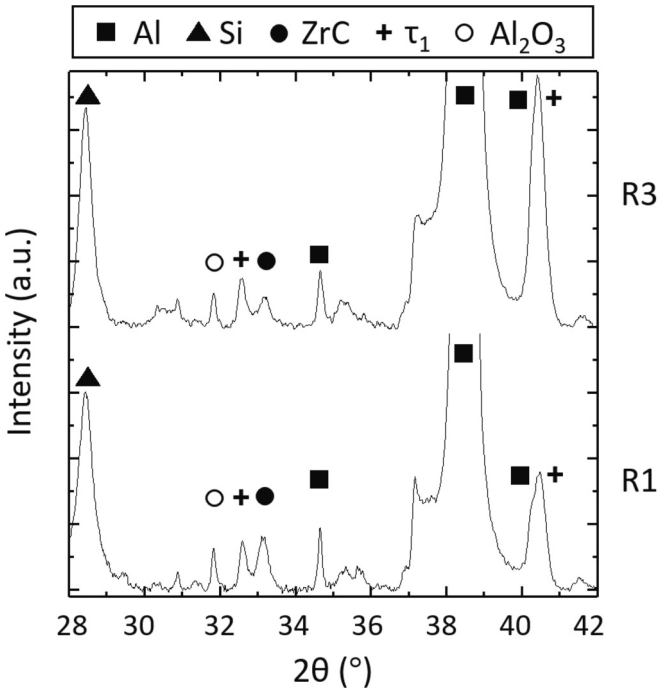

Fig. 3. Composites diffractograms at a EBV of 32.6 J·mm^{-3}.

so the free carbon has probably recombined with aluminum to form Al_4C_3. The TEM analysis shown in Fig. 4 reveals ZrC precipitates by STEM-EDX and electron diffraction, with interreticular distance measurements coinciding with the (2,0,−2), (0,2,−2) et (−2,2,0) planes of the face-centered cubic structure (space group Fm-3 m) of ZrC, with lattice parameter a = 4.68 Å [25]. These precipitates form a necklace of intergranular agglomerated spherical-like nanoprecipitates. The agglomeration of these precipitates supports the hypothesis that only local compositional conditions can enable the formation of the ZrC phase during thermal cycling.

These analyses also reveal residual Al_4C_3 precipitates, with the detection of a carbon-rich precipitate with no Zr or Si signature, as well as both intergranular and intragranular τ_1 phase precipitates, with a morphology mostly in the form of platelets.

The aim now is to identify which of these precipitates is responsible for aluminum germination. As the ZrC phase precipitates as agglomerates, with a heterogeneous and mostly intergranular repartition throughout the material, these precipitates are therefore unlikely to be responsible for germination. On the other hand, as TEM analysis has shown the presence of τ_1 intragranular precipitates, further analysis is carried out to investigate whether the precipitate presents all the criteria for being a good nucleating agent [26,27], starting with a potential orientation relationship between them and the matrix.

This investigation of an orientation relationship is based on a

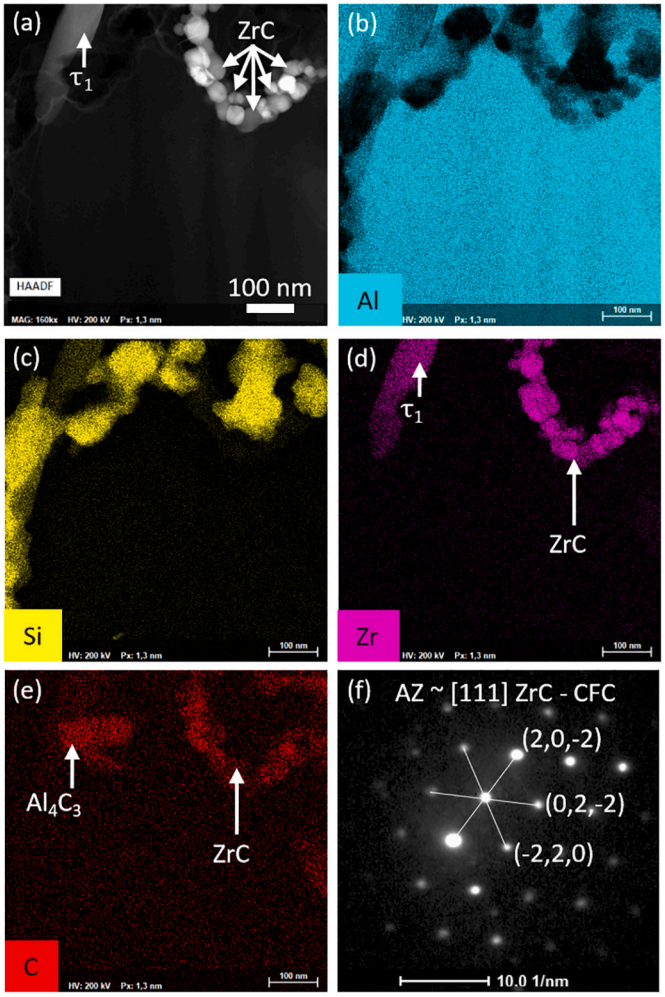

Fig. 4. (a) STEM-HAADF image of precipitates in R1 composite, (b)-(e) STEM-EDX analysis of the same area, (f) Diffraction pattern of a ZrC precipitate oriented along [111] zone axis in the same zone.

comparison of the electron diffraction pattern of the precipitate with that of the matrix surrounding it, using ASTAR [17,18]. Automatic indexing of the diffraction patterns revealed an orientation relationship between the matrix and an intragranular τ_1 precipitate in R3 composite. Fig. 5 provides the EDX analysis of this precipitate, displaying the Si and Zr chemical signatures. The diffraction pattern indexation of the precipitate enables the identification of the (0,−2,0), (−3,−1,2) et (−3,1,2) planes of the quadratic structure of τ_1 phase (space group I4/mmm), whose orientation is close to the [203] zone axis. On the other hand, the face-centered cubic structure of aluminum is oriented close to the [103] zone axis.

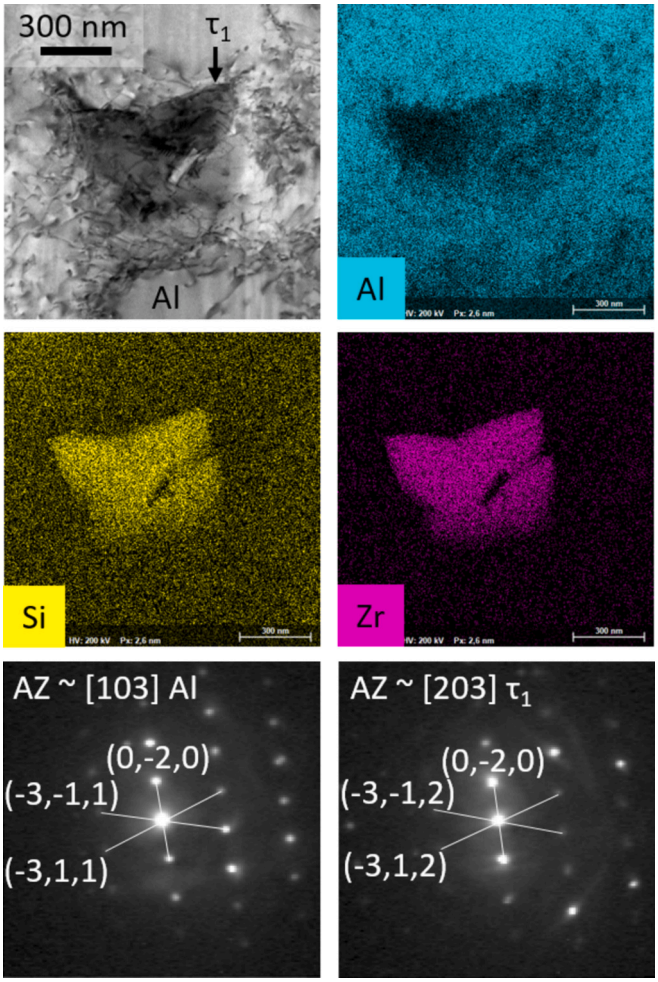

Fig. 5. STEM-EDX analysis of a τ_1 precipitate in R3 composite, with diffraction pattern of the matrix surrounding the precipitate and the τ_1 precipitate.

According to the zone axes identified, the orientations of each of these planes families are plotted in pole figures in Fig. 6 in order to highlight the presence of parallel planes between both structures. The parallel planes between the matrix and the precipitate, highlighted in the pole figures and already suspected from the diffraction images, allow to establish the following orientation relationship: $[103]_{Al}//[203]_{\tau 1}$, $(0,1,0)_{Al}//(0,1,0)_{\tau 1}$, $(-3,-1,1)_{Al}//(-3,-1,2)_{\tau 1}$, $(-3,1,1)_{Al}//(-3,1,2)_{\tau 1}$.

Although encouraging, this observation is as such insufficient to guarantee that the τ_1 phase is a good nucleating agent for the aluminum phase according this orientation relationship. Indeed, the literature indicates several crystallographic criteria that have to be respected [26,27]. Firstly, the parallel planes between both structures must have a small interplanar misfit. Moreover, both structures must have a common dense atomic direction contained within the parallel planes, with a low interatomic distance misfit along this direction. The expression of these misfits is somewhat arbitrarily defined by Wang et al. [26], who propose a limit value of 10 %. To quantify matters, the Vesta software [28] is used to study this orientation relationship from a crystallographic point of view.

The first line in Fig. 7 represents the structures in their respective experimental orientations, each containing the parallel planes previously identified. As the structures are oriented along zone axes, the planes are parallel to the reader's view. The second line of Fig. 7 shows measurements in the (0,1,0) planes of the matrix and precipitate, while the last line concerns the (−3,-1,1) plane of the matrix and the (−3,-1,2) plane of the precipitate. These last two lines show the structures in an orientation that allows the relevant plane to face the reader. On each of these planes, the densest atomic direction is identified, and annotated on the figure. To facilitate the understanding of the figure, the atoms contained in the highlighted planes are circled in dotted lines. Table 4 then presents the values of interplanar and interatomic distance misfits, respectively called f_d and f_r. It reveals that all misfits are below 10 %, and therefore that the orientation relationship detected by TEM allows the τ_1 phase to be a good nucleating agent for the aluminum phase according to the orientation relationship written above.

It is important to mention that this orientation relationship has only been identified for a single precipitate. Nevertheless, it is reasonable to assume that intragranular τ_1-phase precipitates are germinating. On the one hand, electron microscopy analyses have sometimes shown the presence of several Zr-rich precipitates within the same grain, which necessarily implies that all but one of them are not responsible for germination. Furthermore, these analyses showed the presence of Zr-rich precipitates within most grains. Even though such precipitates do not show an orientation relationship with the matrix, they could nevertheless contribute to the reduction of the nucleation energy barrier as foreign particles usually do. In this respect, it should be noted that no other phases that could be candidates for germinating agents were identified. In the same line of thought, the recently proposed Icosahedral Short Range Order (ISRO) nucleation model can be safely ruled out, since TEM analyses did not show the expected high twin densities associated with such a mechanism [29,30].

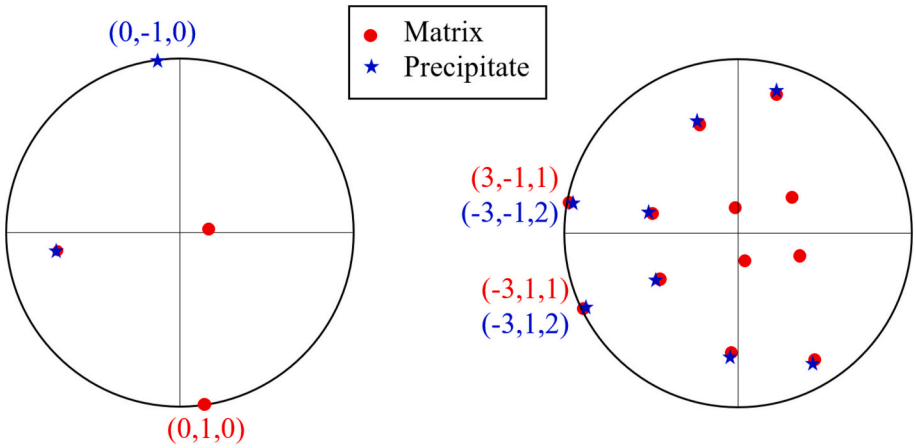

Fig. 6. Pole figures of planes families {1,0,0} for both matrix and precipitate (left), and of planes families {3,1,1} for matrix and {3,1,2} for the precipitate (right).

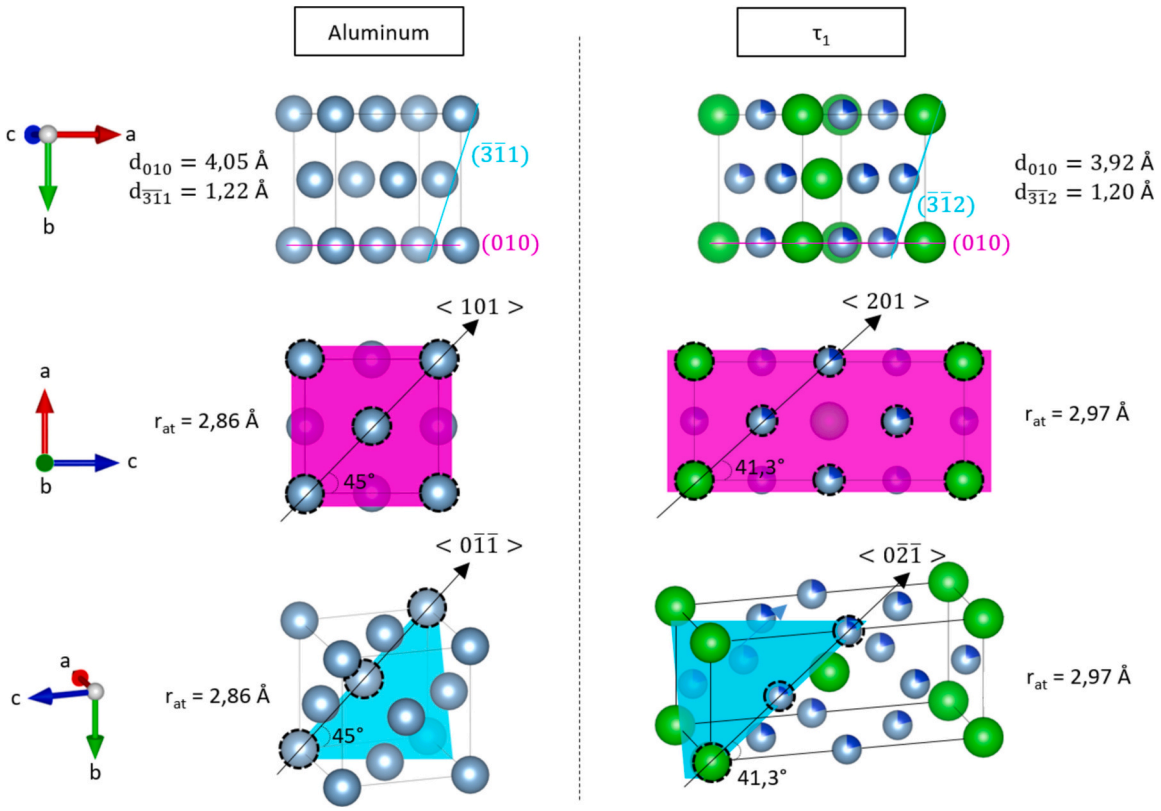

Fig. 7. Crystallographic study of the orientation relationship between matrix and precipitate.

Table 4
Interplanar and interatomic distance misfits.

Parallel planes	$(0,1,0)_{Al}//(0,1,0)_{\tau 1}$	$(-3,-1,1)_{Al}//(-3,-1,2)_{\tau 1}$
f_d	3.41 %	2.26 %
f_r	3.67 %	3.67 %

3.3. Thermodynamics in the Al-Zr-Si-C system

3.3.1. Solidification path

The Al-Zr-Si-C database can be used to follow the formation path of phases during system cooling and solidification. Here, the initial composition is set to match the composition of the R3 composite powder in terms of mass fraction of Si, Zr and C, supplemented by aluminum, as shown in the Table 5.

By calculating the solidification path, the fraction of each phase that will form as the system cools can be predicted. The calculations can be carried out under global (macroscopic) or local (solid-liquid interface) equilibrium conditions. In the latter case, the Scheil-Gulliver model that assumes a homogeneous liquid, no diffusion in the solid and the release of solutes ahead of the growth front, is used. The result presented here relies on the Scheil-Gulliver model, expected to be more representative of rapid solidification conditions, such as those encountered in L-PBF.

The Scheil-Gulliver solidification path is shown in Fig. 8. The first crystalline phase formed during cooling, albeit only to a very small solid fraction, is $Zr_2Al_3C_5$. Next, the τ_1 phase is solidified from 1100 °C to circa 800 °C, before the appearance of the τ_3 phase, defined as $Zr_3Al_4Si_5$

Table 5
Elemental composition (wt%) considered for solidification path calculation.

Element	Al	Si	Zr	C
Mass fraction	Bal.	$7\ 10^{-2}$	$3.34\ 10^{-2}$	$1.47\ 10^{-2}$

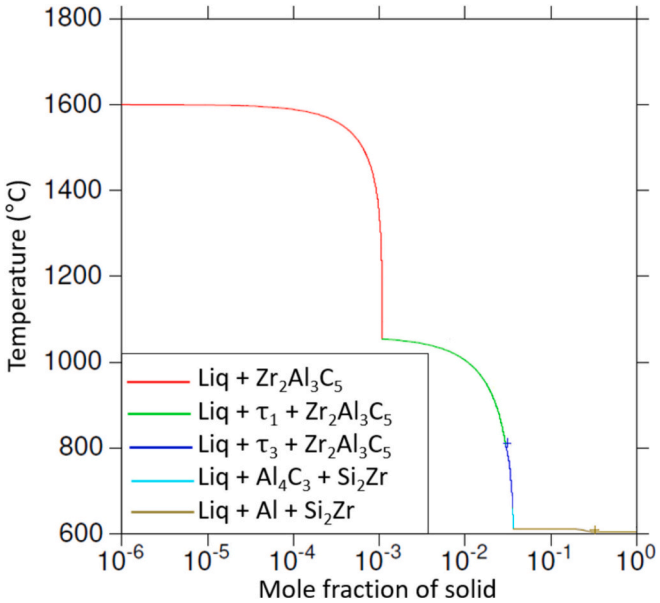

Fig. 8. Solidification path in Scheil-Gulliver condition for R3 composition.

[13]. The calculation then indicates solidification of the Al_4C_3 and Si_2Zr phases from 660 °C, followed by solidification of the aluminum-rich phase.

Regarding the comparison with the experimental results obtained, this solidification path predicts phases that are not observed in practice ($Zr_2Al_3C_5$, τ_3), and also shows that some experimentally formed phases like ZrC are not expected from thermodynamic arguments in the current state of the database. There is therefore no perfect correspondence between experimentally obtained phases and thermodynamics, although

some important similarities are observable, notably through the formation of the τ_1 and Al_4C_3 phases.

Before further analyzing these thermodynamic calculation results in relation to the experimental data previously obtained, heat treatment tests with lower heat transfer kinetics compared to L-PBF process are carried out on the R3 composite powder to support the solidification path results.

3.3.2. *Heat treatments tests with lower kinetics*

Firstly, differential thermal analysis (DTA) tests were carried out on the R3 composite powder, as well as on the reference $AlSi_7Mg_{0.6}$ powder, in order to estimate the formation temperatures of the various phases. The results are qualitatively similar, except for the presence of an exothermic peak observed around 742 °C on the R3 composite powder (see Supplementary data 5).

Then, interrupted thermal treatments on R3 composite at 650 °C and 800 °C allow an XRD identification of the phase formed in this temperature range (Fig. 9).

The τ_1 phase is detected at 800 °C, but not at 650 °C, indicating that the exothermic peak observed at 742 °C is characteristic of the formation of this τ_1 phase, in agreement with the solidification path in Scheil-Gulliver conditions that predicts its precipitation around 800 °C (Fig. 8). Moreover, the $ZrSi_2$ compound, with an orthorhombic crystallographic structure, is detected after both heat treatments. as expected at the end of the solidification path presented above. During heat treatment at 800 °C, the $ZrSi_2$ phase is observed with lower peak intensities than at 650 °C, implying a smaller amount of this compound. The carbides SiC, Al_4C_3 or ZrC are not detected, but it is not however possible to conclude whether this is due to their total absence or their presence in too small quantities. No conclusions can therefore be drawn as to the fate of carbon in these experiments.

4. Discussion

Before turning to a discussion of the relation between experimental observations with the predictions of the thermodynamic model, a number of questions needs to be addressed. In chronological process terms, the first regards the becoming of the ZrO_2 particles and the associated issue of the availability of metallic Zr to form alternative phases needs to be addressed. Indeed, according to the Ellingham diagram, Zr should be a better reducer than Al, meaning that ZrO_2 could be expected to be stable within an aluminum based melt. However,

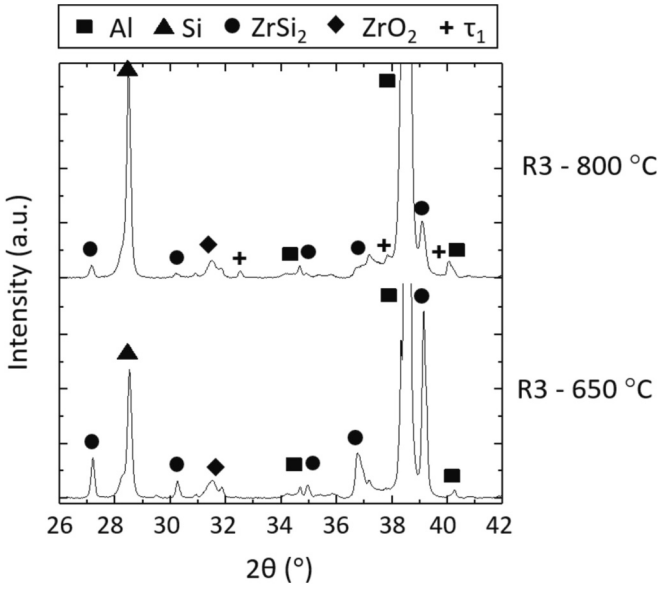

Fig. 9. Heat treated R3 composite powder diffractograms.

preliminary thermodynamic calculations within the (Al-Zr-O) system show that liquid Al is in equilibrium with both Al_2O_3 and ZrO_2 at high temperatures, so that Zr dissolution within the melt is likely. Another option to account for the release of Zr is to invoke the presence of Mg, a very potent reducer, within the alloy composition. As a matter of fact, Mg based oxides had been observed in a previous work [8] on LPBF manufacturing of a related Al 6061 alloy.

Finally a last mechanism would be to consider that at least some of the ZrO_2 particles could melt. The question of the maximum temperature reached during the process is again a tricky one, but values close to the ZrO_2 melting point (circa 2715 °C) are not unreasonable. Furthermore, since the presence of Al in the vicinity of ZrO2 leads to a decrease of the liquidus temperature, a contribution of the melting mechanism to the solubilisation of Zr appears quite likely. In any case, from a practical standpoint, it can be stated that we are fairly confident that a sufficient amount of Zr will be released within the melt. Turning again to our previous work on LPBF manufacturing of a related Al 6061 alloy [8], it was observed that even at a much lower ZrO_2 content within the powder, a large number of Al_3Zr precipitates could be formed in the fabricated parts. Moreover, the observed increase of the intensity of the Al_2O_3 peak on the XRD difractograms is compatible with the trapping by Al of oxygen released from ZrO_2.

Another point that needs to be stated is that, as mentioned before and discussed in detail in our previous publication, a full transformation of SiC into Al_4C_3 was observed for the reference $AlSi_7Mg_{0.6}$-SiC composite material without ZrO_2 addition. Regarding a potential modification of the laser absorption due to the addition of ZrO_2 particles, we did not find evidence of an increase with respect to the reference $AlSi_7Mg_{0.6}$-SiC powders, that would e.g. result in an increase of keyhole porosities at a given energy density. Therefore, it can be safely stated that the reduction of the amount of Al_4C_3 phase after adding ZrO_2 is related to the fact that at least some of the released carbon has been trapped within Zr precipitates.

Regarding the question of whether the amount of intragranular τ1 phase is sufficient to achieve the purpose of grain refinement, characterizations performed on bulk materials did not allow to accurately quantify the density of intra-granular precipitates, a major issue in this respect being that the position of the grain boundaries was often not very clear on the 3D FIB-SEM data. Nevertheless, our in depth observations of a large number of images allow to ensure that τ1 precipitates are visible in most grains, with in some instances more than one precipitate within a given grain. Besides, turning once more to our previous work on LPBF manufacturing of a related Al 6061 alloy [8], it was observed that even at a much lower ZrO_2 content within the powder, the number of Al_3Zr precipitates was largely sufficient to promote equiaxed grain growth. Therefore our opinion is that the amount of intragranular τ1 phase is indeed sufficient for grain refinement purposes.

We now turn to a discussion of the relation between the experimental observations with the predictions of the thermodynamic model, with the objective to better understand the physico-chemical mechanisms involved. Table 6 lists the results obtained in terms of phases in the three situations presented above: L-PBF, heat treatment at 800 °C and thermodynamic calculations.

Firstly, in situ ZrC synthesis is only observed after L-PBF. In this respect, it is important to emphasize that the solidification path calculation is based on the overall composition of the system, and thus may not be able to account for local variations in composition. In the system implemented here, involving a micrometric aluminum powder coated with SiC and ZrO_2 nanoparticles in a process with fast kinetics, this is a limitation to keep in mind. As the hypothesis of ZrC formation is based on local compositional conditions, it was expected that its formation would not be predicted by thermodynamic calculations. Furthermore, the results of experiments aimed at achieving thermodynamic equilibrium (heat treatments) do not show the formation of ZrC.

It is therefore likely that the formation of ZrC in L-PBF was promoted by local compositional conditions on the one hand, and by the kinetic

Table 6
Comparative table of phases obtained with the three methods used.

Method	L-PBF	Heat treatment (800 °C)	Thermodynamic calculations
ZrC	✓	✗	✗
τ_1	✓	✓	✓
Al_4C_3	✓	✗	✓
$ZrSi_2$	✗	✓	✓
$Zr_2Al_3C_5$	✗	✗	✓
τ_3	✗	✗	✓

aspect of the process on the other, which did not allow enough time for the system to reach its thermodynamic equilibrium. A detailed investigation of the convecto-diffusive mass transport mechanisms within the melt pool is far outside the scope of the present work. Nevertheless, it can be thought these mechanisms are not fast enough to instantaneously homogenize the melt, and that the intimate contact between the ZrO2 and SiC additives on top of the AlSi7Mg host particles favors the establishment of process conditions where the formation of ZrC is thermodynamically favored. The 1000 °C isothermal section of the Al-Zr-C phase diagram of Fig. 1(a) indeed shows that for the both R1 and R3 experimental compositions, ZrC is expected to be in equilibrium with Al—Zr intermetallics up to 75 mol% Al.

Again, neither the temperature nor the local compositions within the process can be accurately specified, but it can be safely thought that over a large temperature range the local Al content remains below 75 mol%, thus justifying the formation of ZrC. For industrial applications, it should be noted that, although the formation of ZrC necessarily implies a reduction in the Al_4C_3 content in the parts, its heterogeneous distribution in the material, in the form of agglomerates, will not have the expected impact in terms of mechanical reinforcement.

Then, in line with the predictions of solidification path calculations, the τ_1 phase is observed experimentally after L-PBF, but also after the one-hour heat treatment at 800 °C. Thanks to its role as nucleant, a fine equiaxed microstructure is obtained, instead of a coarser columnar microstructure. Such an equiaxed microstructure could have a beneficial impact on the mechanical properties of composites, promoting isotropic behavior, and with higher performances associated to the numerous grain boundaries acting as obstacles to dislocation movement.

Regarding the $ZrSi_2$ phase, its formation is observed following heat treatment, confirming the results of thermodynamic calculations in the quaternary database. On the other hand, the presence of this $ZrSi_2$ phase was not detected in the samples after L-PBF, which can probably be attributed to the fast kinetics of the process, which did not give this phase time to nucleate, or at least to grow to a measurable amount.

Table 6 then shows the presence of Al_4C_3 after L-PBF, a phase also expected from the solidification path. Local compositional conditions that led to the formation of ZrC, necessarily decreased the available amount of Al_4C_3, but aluminum carbide formation remains expected for the overall system composition. However, as previously indicated, no conclusion can be drawn on the formation of carbide phases during heat treatment due to their absence from XRD diffractograms, which requires characterization at finer but more local scale, complicating the understanding of the composites physicochemistry.

Questions remain about the phases calculated but not obtained or experimentally detected, neither by L-PBF and heat treatments, namely τ_3 and $Zr_2Al_3C_5$. A first assumption is again that they may be present in quantities too small to be detected. Their formation may also be restricted by diffusion kinetics. However, the fact they could not be observed after heat treatments could also point to deficiencies in the database. Indeed, as previously mentioned, the Al-Zr-Si and Al-Zr-C ternary systems suffers from a lack of reliable phase diagram and thermodynamic data.

Finally, the L-PBF results, in line with the solidification path calculation, and by comparison with the heat treatment results, indicate the solidification of the τ_1 phase as well as ZrC and Al_4C_3. On the other hand, the fast kinetics of the L-PBF process limit the formation of the $ZrSi_2$ phase since this phase is observed when the kinetics are slower. Note that the low-temperature equilibrium system does not include the τ_1 phase, so this metastable phase is expected to disappear during thermal annealing in favor of a stable phase at lower temperatures. To check this point, a R3 bulk sample was heat treated for two hours at 500 °C, and the XRD analysis indeed showed the disappearance of the τ_1 phase and the formation of the $ZrSi_2$ phase.

Based on these results, it would be interesting to propose a reaction scheme for the L-PBF processing of an Al-SiC-ZrO_2 composite powder. However, the complexity of the system and the different elements involved in precipitate formation, particularly Zr, make it difficult to take any position. Nevertheless, one could imagine this phases formation reaction scheme in two different situations, depending on the local composition: one with ZrC, the other with Al_4C_3, with τ_1 in both cases. Various reaction mechanisms could be imagined to obtain this final system.

5. Conclusion

This work takes place in the context of the L-PBF elaboration of Al-SiC composites, and more specifically of the thermodynamic instability of SiC in liquid aluminum, leading to the formation of Al_4C_3, a water-soluble carbide that reduces parts lifetime. Our objective was to check the effect of the addition of a source of zirconium to the system to promote the formation of ZrC and thus limit the formation of Al_4C_3.To do so, $AlSi_7Mg_{0.6}$-SiC-ZrO_2 composite powders were elaborated by dry coating and printed in a standard L-PBF equipment. The parts obtained were then thoroughly characterized. In parallel, a first version of a thermodynamic database for the Al-Zr-Si-C system has been set up to help understand the thermochemistry of the composites produced. The main conclusions of this work are summarized as follows:

1- L-PBF processing of $AlSi_7Mg_{0.6}$-SiC-ZrO_2 powder reduces the amount of Al_4C_3 through the formation of ZrC. However, ZrC formation is only possible under local compositional conditions, leading to the formation of ZrC agglomerates, which are a priori not advantageous for the mechanical properties of the parts. Furthermore, Al_4C_3 precipitates can still be observed, even if in smaller quantities.
2- Bulk composites exhibit a fully equiaxed microstructure with a linear grain size of around 1 μm, explained by the precipitation of a nucleating Al-Zr-Si ternary phase named τ_1. Indeed, it displays all characteristics of a good nucleating agent according to the following orientation relationship with the matrix: $[103]_{Al}//[203]_{\tau1}$, $(0,1,0)_{Al}//(0,1,0)_{\tau1}$, $(-3,-1,1)_{Al}//(-3,-1,2)_{\tau1}$.
3- The L-PBF composites microstructures show the precipitation of ZrC, Al_4C_3 and τ_1 phases. Coupled with heat treatment tests with slower kinetics, thermodynamic calculations allow to determine the phases that could be obtained at equilibrium, $ZrSi_2$ and Al_4C_3, after heat treatment of L-PBF materials. These results revealed that the formation of the expected $ZrSi_2$ phase was limited by the L-PBF process kinetics, and that the metastable τ_1 phase disappears in favor of $ZrSi_2$ during heat treatment of a bulk sample from L-PBF.

Regarding perspectives, it would be interesting to study the effect these L-PBF microstructures may have on the mechanical properties of these composites, and to compare them with those of an Al-SiC composite produced by casting and LPBF. These properties could also be compared with those of an $AlSi_7Mg_{0.6}$-ZrO_2 composite by L-PBF, which

would probably allow to obtain an equiaxed microstructure similar to that of the composites developed in this work, without ZrC agglomerates and residual Al_4C_3 precipitates.

Nevertheless, such an objective would require an optimization of the density of the bulk materials obtained after L-PBF. Among the options to be pursued is the drying of the powders before printing, since moisture is known to lead to the formation of occluded gases porosity [31]. In addition, the reinforcement ratio could be optimized, since it has been observed that it is more difficult to obtain dense materials with a high reinforcement ratio. A lower reinforcement ratio is thus expected to lead to density improvements. A more extensive parametric study could also be carried out.

Beyond the scope of this study that focused on the addition of a Zr source, it would also be very interesting to study the effect that the addition of a Ti source could have, since TiC also has a more negative Gibbs energy than Al_4C_3 [6].

Funding

Financial support from the cross-cutting CEA program “Matériaux et Procédés” is gratefully acknowledged. This work, carried out on the Platform for Nanocharacterisation (PFNC), was supported by the “Recherche Technologique de Base” and “France 2030 - ANR-22-PEEL-0014” programs of the French National Research Agency (ANR).

CRediT authorship contribution statement

Marie-Reine Manlay: Writing – original draft, Software, Methodology, Investigation, Data curation, Conceptualization. **Camille Flament:** Writing – review & editing, Supervision, Methodology, Investigation. **Stéphane Gossé:** Writing – original draft, Validation, Software, Methodology. **Mathieu Soulier:** Supervision, Resources, Project administration, Investigation, Funding acquisition, Conceptualization. **Jean-Paul Garandet:** Writing – original draft, Supervision, Methodology, Funding acquisition, Conceptualization.

Declaration of competing interest

The authors declare that they have no known competing financial interests or personal relationships that could have appeared to influence the work reported in this article.

Data availability

Data will be made available on request.

Acknowledgements

The authors would like to thank Laurent Guillem-Guerrero for the 3D printing experiments, Nathalie Ladrat for the FIB lamella preparation and Laurent Chaffron for ATD tests. The authors also acknowledge many fruitful discussions with SIMAP, Univ. Grenoble Alpes, researchers.

Appendix A. Supplementary data

Supplementary data to this article can be found online at https://doi.org/10.1016/j.matchar.2024.114472.

References

[1] J.-F. Silvain, J.-M. Heintz, A. Veillere, Matériaux composites à matrices métalliques, Techniques de l’Ingénieur Matériaux (2018), https://doi.org/10.51257/a-v2-m250.
[2] S.L. Pramod, S. Bakshi, B. Murty, Aluminum-based cast in situ composites: a review, J. Mater. Eng. Perform. 24 (2015), https://doi.org/10.1007/s11665-015-1424-2.
[3] J.C. Viala, P. Fortier, J. Bouix, Stable and metastable phase equilibria in the chemical interaction between aluminium and silicon carbide, J. Mater. Sci. 25 (1990) 1842–1850, https://doi.org/10.1007/BF01045395.
[4] J.K. Park, J.P. Lucas, Moisture effect on SiCp/6061 Al MMC: dissolution of interfacial Al4C3, Scr. Mater. 37 (1997) 511–516, https://doi.org/10.1016/S1359-6462(97)00133-4.
[5] M.-R. Manlay, J.-P. Garandet, G. Bacchetta, M. Soulier, C. Flament, On the elaboration of composite AlSi7Mg0.6/SiC powders and parts by laser powder bed fusion, J. Mater. Sci. 58 (2023) 5269–5286, https://doi.org/10.1007/s10853-023-08249-1.
[6] J. Long, L.-J. Zhang, L.-L. Zhang, X. Wang, G.-F. Zhang, J.-X. Zhang, S.-J. Na, Effects of minor Zr addition on the microstructure and mechanical properties of laser welded joint of Al/SiCp metal-matrix composite, J. Manuf. Process. 49 (2020) 373–384, https://doi.org/10.1016/j.jmapro.2019.12.004.
[7] J.C. Schuster, H. Nowotny, Investigations of the ternary systems (Zr, Hf, Nb, Ta)-Al-C and studies on complex carbides, Z. Metallkde. Bd. 71 (1980) 341–346.
[8] M. Opprecht, J.-P. Garandet, G. Roux, C. Flament, M. Soulier, A solution to the hot cracking problem for aluminium alloys manufactured by laser beam melting, Acta Mater. 197 (2020) 40–53, https://doi.org/10.1016/j.actamat.2020.07.015.
[9] M. Genc, P. Eloi, J.-J. Blandin, C. Pascal, P. Donnadieu, F. De Geuser, P. Lhuissier, C. Desrayaud, G. Martin, Optimization of the strength vs. conductivity trade-off in an aluminium alloy designed for laser powder bed fusion, Mater. Sci. Eng. A 858 (2022) 144139, https://doi.org/10.1016/j.msea.2022.144139.
[10] A. Mehta, L. Zhou, T. Huynh, S. Park, H. Hyer, S. Song, Y. Bai, D.D. Imholte, N. E. Woolstenhulme, D.M. Wachs, Y. Sohn, Additive manufacturing and mechanical properties of the dense and crack free Zr-modified aluminum alloy 6061 fabricated by the laser-powder bed fusion, Addit. Manuf. 41 (2021) 101966, https://doi.org/10.1016/j.addma.2021.101966.
[11] X. Nie, H. Zhang, H. Zhu, Z. Hu, L. Ke, X. Zeng, Effect of Zr content on formability, microstructure and mechanical properties of selective laser melted Zr modified Al-4.24Cu-1.97Mg-0.56Mn alloys, J. Alloys Compd. 764 (2018) 977–986, https://doi.org/10.1016/j.jallcom.2018.06.032.
[12] Takayuki Hirano, Hiroshi Ohtani, Mitsuhiro Hasebe, Thermodynamic analysis of the Al-Si-Zr ternary system, High Temp. Mater. Processes 29 (2010) 347–372, https://doi.org/10.1515/HTMP.2010.29.5-6.347.
[13] Y. Liu, M. Tang, C. Wu, J. Wang, X. Su, Progress on phase equilibria of the AlSiZr system at 700 and 900 °C, J. Alloys Compd. 693 (2017) 357–365, https://doi.org/10.1016/j.jallcom.2016.09.142.
[14] R. Pfeffer, R.N. Dave, D. Wei, M. Ramlakhan, Synthesis of engineered particulates with tailored properties using dry particle coating, Powder Technol. 117 (2001) 40–67, https://doi.org/10.1016/S0032-5910(01)00314-X.
[15] M. Soulier, A. Benayad, L. Teulon, Y. Oudart, S. Senol, K. Vanmeensel, Nanocomposite powder for powder-bed-based additive manufacturing obtained by dry particle coating, Powder Technol. 404 (2022) 117474, https://doi.org/10.1016/j.powtec.2022.117474.
[16] M.C. Sow, T. De Terris, O. Castelnau, Z. Hamouche, F. Coste, R. Fabbro, P. Peyre, Influence of beam diameter on laser powder bed fusion (L-PBF) process, Addit. Manuf. 36 (2020) 101532, https://doi.org/10.1016/j.addma.2020.101532.
[17] E.F. Rauch, J. Portillo, S. Nicolopoulos, D. Bultreys, S. Rouvimov, P. Moeck, Automated nanocrystal orientation and phase mapping in the transmission electron microscope on the basis of precession electron diffraction, Z. Krist. 225 (2010) 103–109, https://doi.org/10.1524/zkri.2010.1205.
[18] E.F. Rauch, M. Véron, Automated crystal orientation and phase mapping in TEM, Mater Charact 98 (2014) 1–9, https://doi.org/10.1016/j.matchar.2014.08.010.
[19] J. Gröbner, H.L. Lukas, F. Aldinger, Thermodynamic calculation of the ternary system Al-Si-C, Calphad 20 (1996) 247–254, https://doi.org/10.1016/S0364-5916(96)00027-2.
[20] A. Fernández Guillermet, Analysis of thermochemical properties and phase stability in the zirconium-carbon system, J. Alloys Compd. 217 (1995) 69–89, https://doi.org/10.1016/0925-8388(94)01310-E.
[21] A. Poulou, T.A. Mellan, M.W. Finnis, Stability of Zr-Al-C and Ti-Al-C MAX phases: a theoretical study, Phys. Rev. Mater. 5 (2021) 033608, https://doi.org/10.1103/PhysRevMaterials.5.033608.
[22] H.M. Chen, Y. Xiang, S. Wang, F. Zheng, L.B. Liu, Z.P. Jin, Thermodynamic assessment of the C–Si–Zr system, J. Alloys Compd. 474 (2009) 76–80, https://doi.org/10.1016/j.jallcom.2008.06.086.
[23] M.-R. Manlay, Contribution à la compréhension de la physico-chimie de composites carburés à matrice aluminium élaborés par fusion laser sur lit de poudre, Science des matériaux, Université Grenoble Alpes, 2023, pp. 183–184. ⟨NNT : 2023GRALI083⟩, ⟨tel-04414946⟩.
[24] T. Gao, X. Cui, X. Li, H. Li, X. Liu, Morphological evolutions and growth patterns of Zr-containing phases in aluminum alloys, CrystEngComm 16 (2014) 3548, https://doi.org/10.1039/c3ce42548g.
[25] A.R. Mallick, S. Chakraborty, P.K. Das, Synthesis and consolidation of ZrC based ceramics: a review, Rev. Adv. Mater. Sci. 44 (2016) 109–133.
[26] F. Wang, D. Qiu, Z. Liu, J. Taylor, M. Easton, M. Zhang, Crystallographic study of Al3Zr and Al3Nb as grain refiners for Al alloys, Trans. Nonferrous Met. Soc. Chin. 24 (2014) 2034–2040, https://doi.org/10.1016/S1003-6326(14)63309-4.
[27] Q. Tan, J. Zhang, Q. Sun, Z. Fan, G. Li, Y. Yin, Y. Liu, M.-X. Zhang, Inoculation treatment of an additively manufactured 2024 aluminium alloy with titanium nanoparticles, Acta Mater. 196 (2020) (2024) 1–16, https://doi.org/10.1016/j.actamat.2020.06.026.
[28] K. Momma, F. Izumi, VESTA : a three-dimensional visualization system for electronic and structural analysis, J. Appl. Cryst. 41 (2008) 653–658.

[29] M. Rappaz, Ph. Jarry, G. Kurtuldu, J. Zollinger, Solidification of metallic alloys: does the structure of the liquid matter? Metall. Mater. Trans. A 51 (2020) 2651–2664, https://doi.org/10.1007/s11661-020-05770-9.
[30] C. Galera-Rueda, M.L. Montero-Sistiaga, K. Vanmeensel, M. Godino-Martínez, J. Llorca, M.T. Pérez-Prado, Icosahedral quasicrystal-enhanced nucleation in Al alloys fabricated by selective laser melting, Addit. Manuf. 44 (2021) 102053, https://doi.org/10.1016/j.addma.2021.102053.
[31] X.P. Li, K.M. O'Donnell, T.B. Sercombe, Selective laser melting of Al-12Si alloy: enhanced densification via powder drying, Addit. Manuf. 10 (2016) 10–14, https://doi.org/10.1016/j.addma.2016.01.003.